Two-dimensional measurements of laser-induced breakdown in air by high-speed two-frame shadowgraphy

Peter Gregorčič · Janez Diaci · Janez Možina

Abstract We present two-dimensional measurements of the laser-induced plasma development and shock wave evolution in air. The breakdown is induced by a Q-switched Nd:YAG laser ($\lambda = 1064$ nm) with a pulse duration of 4 ns. To study these fast laser-induced phenomena, we have developed a high-speed, two frame shadowgraph method. It enables 2D visualization of a laser-induced event in two time instances, which are delayed by an arbitrary time interval in the range from 300 ps to 30 ns. The established method is based on 30 ps, green ($\lambda = 532$ nm), and linearly polarized laser pulse, which is split into two orthogonally polarized illumination pulses for direct and delayed illumination of the breakdown area. Exploiting polarization of the probe pulses, we capture two temporally and spatially separated frames with two CCD cameras. Special attention is given to the subsequent data processing, especially to the minimization of the systematic error due to alignment of both images, and to the determination of 2D velocity distribution from the captured image pairs.

1 Introduction

A high-intensity laser pulse ($>10^{14}$ W/m^2) in the nanosecond range that is focused into gasses or liquids, forms plasma due to optical breakdown [1–3]. Such a plasma is a strong absorber of the laser light. Thus, high temperatures and high pressures are rapidly created [4] and due to plasma shielding the plasma plume explosively expands mainly toward the focusing lens [5] with a supersonic velocity. It

was shown in [6] that in ambient air the nanosecond-laser-induced breakdown initiates at different points within the excitation-beam volume. High-pressures drive intense blast waves that expand from these local centers and combine within the excitation pulse into a single shock wave, which propagates into the surrounding gas. Finally, i.e., after few tens of microseconds, this shock wave decays into the acoustic wave motion. In such an optodynamical process, the optical energy of the excitation-laser pulse is converted into the mechanical energy of the shock wave that propagates into the surrounding medium [7]. Such optodynamic phenomena contain important information about the laser-material interaction, therefore, their detection and analysis is of great importance in many industrial [8, 9] and medical [10, 11] applications.

The analysis of the process of the laser-induced phenomena requires the observation of the initial states of the plasma formation, plasma expansion, and shock wave development as well as the shock wave propagation and its decay into an acoustic wave motion. There are several optical methods used for the characterization of different stages of the laser-induced breakdown, such as shadow and schlieren photography [12–15], high-speed photography [16], streak photography [17], holography [18], measurements based on a laser-beam deflection probe [19, 20], laser-induced breakdown spectroscopy [21], and a combination of these methods [22, 23].

The main goal of our study was to develop a method that enables 2D measurements of instantaneous velocities of fast optodynamic phenomena. Such measurements are especially important in many laser-assisted applications, where the shock-wave peak pressure, which is a crucial parameter, is related to the shock-wave propagation speed [24]. Therefore, our high-speed, two-frame shadowgraph method enables 2D visualization of a single optical breakdown event

P. Gregorčič (✉) · J. Diaci · J. Možina
Faculty of Mechanical Engineering, University of Ljubljana, Aškerčeva 6, 1000 Ljubljana, Slovenia
e-mail: peter.gregorcic@fs.uni-lj.si

in two time instances [6]. The method is based on 30-ps, linearly polarized pulse, which is split into two orthogonally polarized probe pulses for the direct and delayed illumination of the breakdown area. Using an optical delay line, a variable delay between the direct and the delayed illumination can be achieved in the range between 300 ps and 30 ns. The established method presents an accessible solution for many industrial and medical research environments, where temporally and spatially observation of different kinds of laser-induced phenomena in all kinds of transparent media is required.

In this contribution, we describe the developed shadowgraph method and subsequent data processing based on the analysis of image pairs acquired during a single breakdown event. Such an analysis allows the determination of 2D velocity fields of the breakdown area. We show that our method enables the shadowgraphic observation of all stages of laser-induced breakdown including the breakdown initiation and plasma development within the irradiation with the excitation-laser pulse. The main focus of the presented experiments are the 2D measurements of instantaneous velocities of plasma and shock-wave evolution in air from the very beginning of the laser-induced breakdown to the times, when the shock wave decays into an acoustic wave. By way of these measurements, we demonstrate and discuss the capability of the presented shadowgraph method.

2 Experimental setup

The top view of our high-speed, two-frame shadowgraph method for observation of the laser-induced breakdown is schematically shown in Fig. 1. The breakdown in ambient air is induced by a Q-switched Nd:YAG laser ($\lambda = 1064$ nm,

Quantel, France, Brio) employed as the excitation source. It emits 4-ns (FWHM) pulses with energy $E_L = 12.7$ mJ $\pm$ 0.5 mJ and peak power $P_L = 2.9$ MW $\pm$ 0.5 MW after the attenuator (A). Since the excitation beam is partially reflected by the polarizer inside the attenuator, its energy can be simultaneously measured by the energy meter (E) during the experiments. After the attenuator, the excitation beam is guided through the beam expander (BE) and focused by the lens (L) with a focal length of 120 mm to a diameter of 25 μm in air. Thus, in the focus, it achieves the peak intensity around 6×10^{15} W/m^2, which is just above the threshold intensity. i.e., $I_{th} \approx 5 \times 10^{15}$ W/m^2.

The laser-induced breakdown in air is examined using high-speed, two-frame shadowgraphy. Here, a frequency-doubled Nd:YAG laser (Ekspla, Lithuania, PL2250-SH-TH) emitting green ($\lambda = 532$ nm) pulses with duration of 30 ps (FWHM) is used as an illumination source. After the half-wave plate (HWP), the illumination-beam polarization forms a 45° angle with respect to the optical table. The first polarizing beam splitter (PBS) is used to divide the single illumination-pulse into two pulses with perpendicular linear polarizations. The x-polarized pulse (the direct probe) hits the breakdown area directly, while the y-polarized pulse (the delayed probe) passes an optical delay line before hitting the breakdown area. By using the second PBS, both probe-pulses illuminate the breakdown region along the same path. Before the breakdown area, the probes are expanded with the BE. A narrow band-pass filter (BPF) centered at 532 nm $\pm$ 10 nm is placed between the breakdown region and the microscope to block the light emitted from plasma. Another PBS is placed inside the microscope, where it transmits the direct (x-polarized) probe to the CCD camera Cx and reflects the delayed (y-polarized) probe to the CCD camera Cy. In such a way, we use the polarization of both probes to capture two temporally and spatially

Fig. 1 Schematic top view of the high-speed, two-frame shadowgraphy
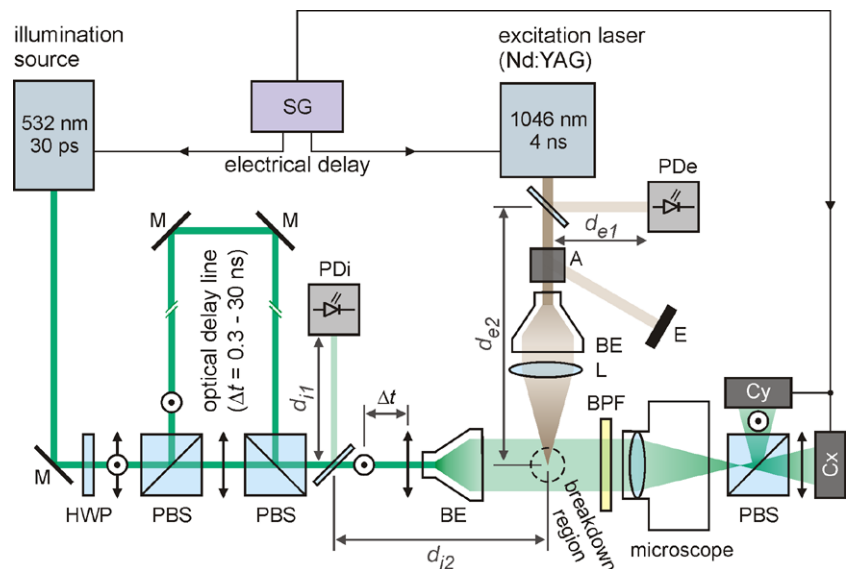
separated frames with two CCD cameras (Basler AG, Germany, scA1400-17fm, 1.4 Mpx). The spatial resolution of our optical system is in the range of $\kappa = 0.7$–1.5 µm/px. For a particular series of measurements, κ value was determined using images of a calibrating pattern.

The probe pulses are delayed by an *optical delay line*. In our case, the path of the delayed probe is 0.1–10 m longer than the path of the direct probe. Therefore, we can produce an arbitrary time delay, Δt, between the probes in the range from 300 ps to 30 ns. Here, the shortest time delay, Δt, is theoretically limited by the illumination-pulse duration, but practically it should be at least 1 order of magnitude longer. On the other hand, the longest time delay between probe-pulses is limited by the stability of the optical components in the delay line. Since the accuracy of the path of the delay line is around 1 mm, the uncertainty of the time delay between both probes is less than 10 ps.

The lasers and cameras are synchronized with a signal generator (SG) connected to a personal computer. Therefore, the time delay, t_1, between the illumination and excitation source is defined by an *electric delay* produced by the SG. This delay between lasers has been chosen in the range from -10 ns to 20 µs in steps of 1 ns. Resolution down to 100 ps has been achieved by repeated measurements exploiting jitter of this synchronization, which is ± 6 ns.

The illumination and excitation pulses are partially reflected by dielectric plates to the fast photodiodes PDi and PDe, respectively. The used photodiodes with a bandwidth of 1 GHz have a rise time of 600 ps. Assuming that the coaxial cables from both photodiodes to the oscilloscope (LeCroy, US, 600 MHz Wave Runner 64MXi-A, a sampling rate of 10 GS/s) are of equal length, the time delay, t_1, between the direct-probe pulse and the excitation pulse at the breakdown region can be calculated as

$$t_1 = \Delta t_{PD} + \frac{d_{i2} - d_{i1} + d_{e1} - d_{e2}}{c}. \tag{1}$$

Here, Δt_{PD} stands for the delay between the signals acquired from PDi and PDe; d_{i1}, d_{e1} are the distances between the dielectric plates and photodiodes PDi and PDe, respectively; d_{i2}, d_{e2} are the distances between the dielectric plates and the breakdown region (see Fig. 1); and c is the speed of light in the air. Time t_1 corresponds to the time of directly exposed image captured by camera Cx, while the time of the delayed exposure t_2, captured by camera Cy, can be calculated as $t_2 = t_1 + \Delta t$.

The experimental setup is controlled with custom developed software that enables the data acquisition from a digital oscilloscope and subsequent signal processing as well as the image acquisition from cameras. In the offline processing, this software is also used for the subpixel alignment of captured images and subsequent image processing, described in the next section.

3 Data processing

The measurements of the optical breakdown by the described method are based on the image pairs, which are acquired during a single breakdown event. The shutters of the two cameras are open during the measurements, while two 30-ps-long illumination pulses hit the breakdown region at times t_1 and t_2. An example of such image pair is shown in Fig. 3a. Since typical pairs of images captured by different time delays, Δt, are presented in detail in our previous work [6], we will restrict ourselves here to the description of data processing. Here, the main emphasis is given to (i) the minimization of the systematic error due to alignment of both images; and (ii) the determination of 2D velocity distribution from captured image pairs.

3.1 Image pair alignment

Before the measurements, the cameras are mechanically aligned. A typical image pair showing the alignment of cameras is presented in Fig. 2a. Here, we use the setup sketched in Fig. 1, where the cross-pattern printed on a paper is placed

Fig. 2 Software alignment of image pairs. (**a**) The cross-pattern captured by both cameras after the mechanical alignment. (**b**) The determination of the cross-pattern captured by Cx (the *blue dots*) and Cy (the *red dots*). The fitted linear functions to these *dots* (the *broken lines*) are used to obtain the spatial transformation of image from Cy
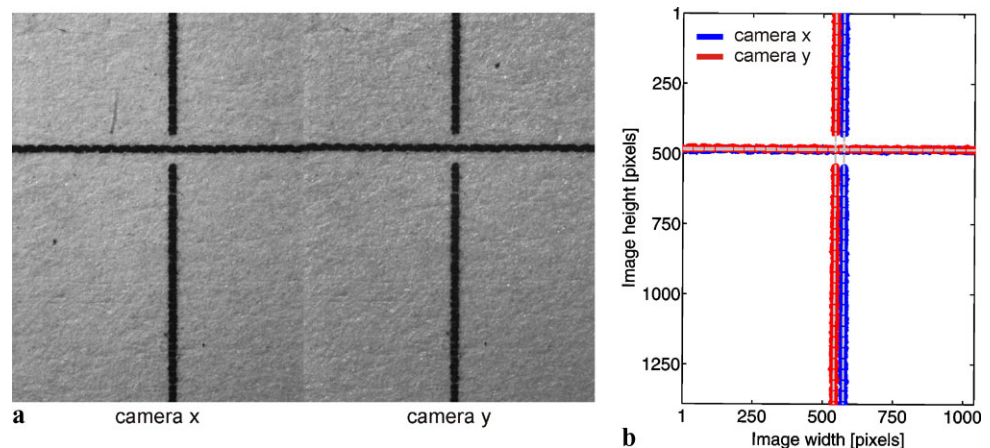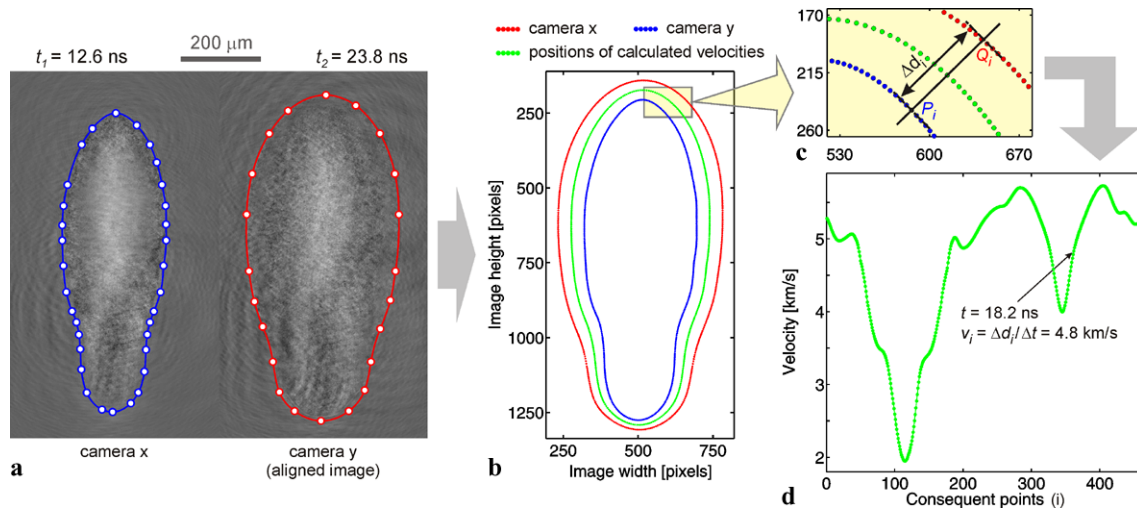
Fig. 3 The procedure for determination of 2D velocity distribution. (**a**) Typical image pair showing the shock wave at times t_1 and t_2. The *solid lines* show Bézier splines, while the control points are marked with the *white points*. (**b**) The boundaries of the shock wave captured by Cx (the *blue points*) and Cy (the *red points*). The *green points* show the position of the calculated velocities. (**c**) Determination of the distance Δd_i. (**d**) Calculated velocities for each point P_i

in the breakdown region and illuminated by a light from the front side. The comparison between images from Cx and Cy in Fig. 2a reveals that the same pattern is placed at different positions in the images. Therefore, one of both images should be software-aligned (translated and rotated) during data processing to avoid the systematic error of calculated velocities. To do this, we first use the image processing to determine the cross-pattern captured by Cx (the blue dots in Fig. 2b) and Cy (the red dots in Fig. 2b). Then the linear functions are fitted to dots representing the horizontal (the full line in Fig. 2a) and vertical (the broken line in Fig. 2a) lines of this pattern. The fitted linear functions are shown as broken lines in Fig. 2b. From the intersections and the slopes of these functions, we determine the spatial transformation (translation and rotation). Using this transformation, we transform the image from Cy by a bilinear interpolation algorithm so that it is aligned with the image from Cx with a subpixel accuracy.

3.2 Determination of 2D velocity distribution

The 2D velocity distribution is calculated from shock wave boundaries in the image pair. The procedure for determination of the 2D velocity distribution is presented in Fig. 3. Figure 3a shows a typical image pair captured at $t_1 = 12.6$ ns with the optical delay between probe pulses $\Delta t = 11.2$ ns. The shape of the shock wave is first approximated by a Bézier spline [25], i.e., a series of cubic Bézier curves joined end to end in the control points. The control points (the white points in Fig. 3a) are manually selected so that the Bézier spline (the blue and the red line in Fig. 3a) coincides with the shape of the shock wave.

In Fig. 3b, the blue points correspond to the boundary of the shock wave captured with the Cx, while the red points represents the spline showing the shock wave captured $\Delta t = 11.2$ ns later with the Cy. For each point, P_i, at the boundary of the Cx (the blue points in Fig. 3b), the velocity v_i is calculated as

$$v_i = \frac{\Delta d_i}{\Delta t}\kappa. \tag{2}$$

In Eq. (2), i stands for the index of each point, the distance Δd_i equals the shift (in pixels) of the point P_i during the time interval Δt, and κ is the spatial resolution of the optical system.

The shift Δd_i is determined from the captured images as is shown in Fig. 3c. First, the normal to the spline at the point $P_i = (x_{P_i}, y_{P_i})$ is calculated. The corresponding point $Q_i = (x_{Q_i}, y_{Q_i})$ at the Cy is determined as the intersection between this normal and the spline describing the shape of the shock wave captured at t_2. The distance (in pixels) between points P_i and Q_i is calculated as

$$\Delta d_i = \sqrt{(x_{Q_i} - x_{P_i})^2 + (y_{Q_i} - y_{P_i})^2}, \tag{3}$$

while the time t and the position d_i of the calculated velocity v_i are determined as

$$\{t, d_i\} = \left\{ \frac{t_1 + t_2}{2}, \left(\frac{x_{P_i} + x_{Q_i}}{2}, \frac{y_{P_i} + y_{Q_i}}{2} \right)\kappa \right\}. \tag{4}$$

After the above procedure, we have the position of the shock wave boundary at time t (the green points in Fig. 3b) and the 2D distribution of its velocities. The calculated velocities for each point P_i are presented in Fig. 3d.

Fig. 4 2D velocity distribution. (**a**) The shapes of the shock waves at selected times t. The shock waves have aligned the geometric centers. (**b**) The velocity as a function of angle, defined in (**a**)
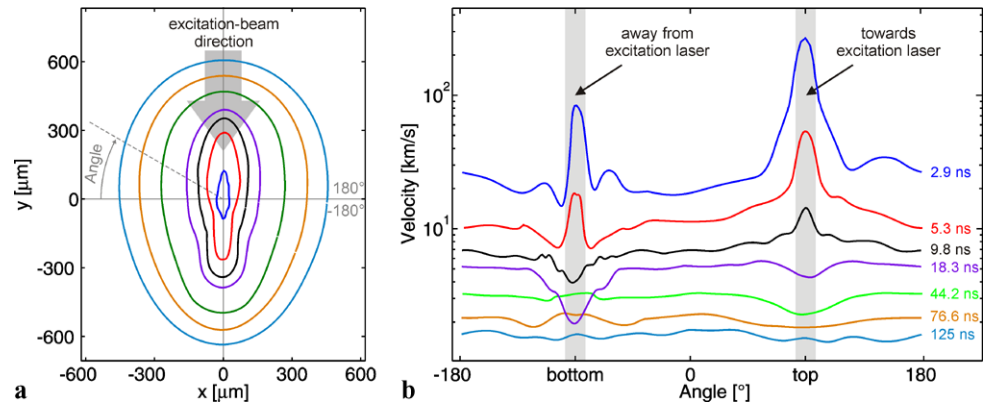

4 Results and discussion

The described data processing was used to obtain 2D velocity distribution of the shock wave propagation at different times t. The measured velocities for selected times are presented in Fig. 4. Figure 4a shows the shapes of the shock wave at $t = \{2.9 \text{ ns}, 5.3 \text{ ns}, 9.8 \text{ ns}, 18.3 \text{ ns}, 44.2 \text{ ns}, 76.6 \text{ ns}, 125 \text{ ns}\}$, where $t = 2.9$ ns corresponds to the innermost shock wave. In order to show the calculated velocity as a function of angle, the geometric centers of shock waves in Fig. 4a are manually aligned. Dimensions of the CCD sensor limit the maximum dimension of the captured phenomenon at a particular spatial resolution κ. For this reason, the κ values have been increased from 0.7 µm/px for the innermost to 1.5 µm/px for the outermost shock wave in Fig. 4a.

Figure 4b shows the velocities of each measured shock wave as a function of angle (defined in Fig. 4a). Here, the 90° angle corresponds to the top of the shock wave, i.e., its part that propagates *toward* the excitation laser. Vice versa, the −90° angle corresponds to the bottom of the shock wave, which propagates *away from* the excitation laser. Immediately after the breakdown, the top and the bottom of the shock wave have much higher velocities than its left and right side. This results in the ellipsoidal shape. It can be seen from Fig. 4b that the bottom has lower velocity during the excitation-laser radiation ($t < 10$ ns) due to strong absorption of the laser light in the plasma, resulting in plasma shielding. The velocity peaks at ±90° disappear after the end of the excitation pulse. Moreover, the velocities of these peaks at $t = 18.3$ ns are lower than the velocities in the horizontal directions (0° and 180°). Due to this reason, the ellipsoidal shock wave converts into a shock wave with a spherical shape. More than 100 ns after the breakdown the velocity as a function of angle is approximately constant as it is evident from the bottom two curves in Fig. 4b.

In order to present the capabilities and limitations of the developed method, we have measured the axial velocities toward the focusing lens (i.e., the velocities at angle 90° in Fig. 4). These velocities as a function of time are presented in a log–log plot in Fig. 5. Here, the inset shows the
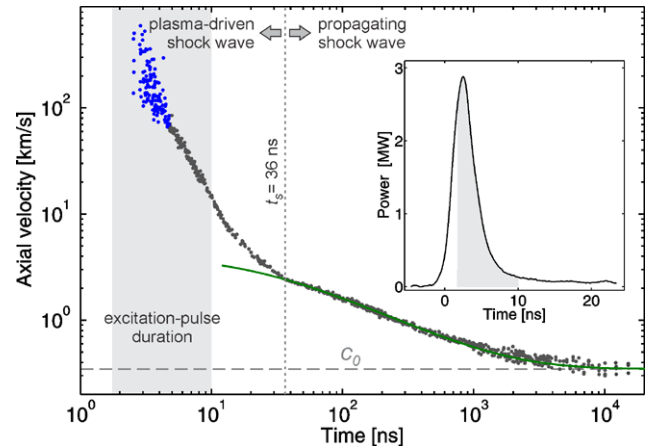
Fig. 5 Axial velocity of the shock wave development toward the excitation laser as a function of time t. The *green solid curve* is the fit of Eq. (5) to the data measured at times $t > t_s$. The *inset* shows the power of an excitation-laser beam as a function of time

power of the excitation pulse versus time and the time zero corresponds to the triggered value of the excitation-pulse power. From the inset in Fig. 5, it can be estimated that the power threshold in our case is around $P_{th} \approx 2.6$ MW. For our spot size, this matches the intensity threshold around $I_{th} \approx 5 \times 10^{15}$ W/m², which is in agreement with values listed in the literature [3, 26]. The shaded area in Fig. 5 as well as in the inset shows the time interval during the excitation-laser radiation.

Within the first two nanoseconds after the breakdown initiation (i.e., in the time interval from $t \sim 2.5$ ns to $t \sim 5$ ns), the measured axial velocities of the edge of the plasma plume vary from 600 km/s to 100 km/s, which conforms with the ionization front velocities presented elsewhere [4]. Here, a significant measurement noise (the blue points in Fig. 5) arises from the different mechanisms of plasma expansion [4, 5]. The higher velocities (i.e., greater than 250 km/s) are recorded during fast ionization, while the lower axial velocities are related to the events captured during the laser-supported detonation wave. When the excitation-pulse power becomes too low to allow air ioniza-

tion ($t > 5$ ns), the fast ionization phase ends and the measurement noise in Fig. 5 is significantly reduced. However, the shock wave is still plasma-driven and its shape is ellipsoidal (see Fig. 4a), as has been already shown by many authors (e.g., see [8, 27]). In the time interval from $t \sim 5$ ns to $t \sim 10$ ns, the plasma energy still increases due to the absorption of the laser-radiation. When the excitation-laser radiation ends ($t > 10$ ns), the high-temperature plasma drives the shock wave, thus prolonging its explosive expansion. This ends at $t_s = 36$ ns, when the shock wave energy becomes constant (if the energy dissipation is negligible) and the ellipsoidal shape of the shock wave is converted into a nearly spherical shape, as can be seen in Fig. 4a (see also [27]).

The Jones theory for the intermediate strength blast wave [24] can be employed to describe propagation of the shock wave past t_s. The solid line in Fig. 5 represents the fitted theoretical velocity derived from the model for the spherical blast wave [24]:

$$v(t; E_0, t_0)$$
$$= c_0 \frac{(1 + (\frac{5}{2})^{2/3} c_0 (\lambda_S^5 \frac{E_0}{\gamma p_0})^{-1/3} (t - t_0))^{3/2}}{((1 + (\frac{5}{2})^{2/3} c_0 (\lambda_S^5 \frac{E_0}{\gamma p_0})^{-1/3} (t - t_0))^{5/2} - 1)^{3/2}}. \quad (5)$$

Here, the energy of the shock wave E_0 and the time offset t_0 are the fitting parameters. In Eq. (5), the p_0 is the ambient pressure, $\gamma = 1.4$ is the specific-heat ratio, $\lambda_S^5 = 1.175$ is a dimensionless geometry-dependent parameter [28, 29], and $c_0 = 346$ m/s is the speed of sound in air for the ambient conditions ($p_0 = 10^5$ Pa, $T_0 = 25$ °C).

Equation (5) is valid for the point explosion, where the whole energy is released at once at time $t = 0$. In our case, the energy of the shock wave increases during the plasma expansion. This is the reason that we have added an additional fitting parameter, t_0 into Eq. (5). For the same reason, the model is fitted only to the data measured at $t > t_s$. In such a way, we obtain the energy $E_0 = 1.68$ mJ ± 0.5 mJ of the laser-induced shock wave. From the energy of the laser pulse, it can be concluded that in our case the portion $\eta = E_0/E_L = 13$ % ± 1 % of the excitation-beam energy was converted into the mechanical energy of the shock wave. This result is in agreement with the results presented by Diaci and Možina [30], who have also shown that the energy-conversion efficiency increases with the excitation-pulse energy.

Measurement uncertainty of the presented method and set-up can be estimated from Eq. (2):

$$\frac{\delta v_i}{v_i} = \left| \frac{\delta \Delta d_i}{\Delta d_i} \right| + \left| \frac{\delta \Delta t}{\Delta t} \right| + \left| \frac{\delta \kappa}{\kappa} \right|, \quad (6)$$

where the right-hand side fractions denote relative measurement uncertainties of the respective measured quantities. We estimate the last term in the right-hand side of Eq. (6) to be less than 1 %, while the value of $\delta \Delta t / \Delta t$ is up to 3 %.
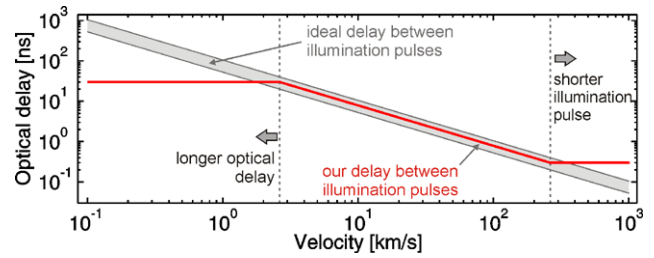
Fig. 6 The optical delay Δt between probe pulses as a function of the shock wave velocity. The optimal delay (calculated from Eq. (2)) is shown by the *gray-shaded region*. *The red line* shows the optical delay during our measurements

The measurement uncertainty $\delta \Delta d_i$ is around five pixels. To keep the value of the first term in the right-hand side of Eq. (6) less than 10 %, we were adapting during our measurements the optical delay Δt between probe pulses so that the Δd_i was in the range between 75 and 150 pixels. Here, it should be noted that too short delay line increases relative error due to the error of the shock wave boundary detection. On the other hand, when an inappropriately long optical delay is used, the measured average velocity does not conform to the instantaneous velocity of the measured phenomena. An optimal optical delay, Δt, as a function of the propagation velocity is shown by the gray-shaded region in Fig. 6. The upper and the bottom limits are determined from Eq. (2) for $\Delta d_i = 70$ pixels and $\Delta d_i = 150$ pixels, respectively. Here, the spatial resolution of optical system $\kappa = 0.7$ μm/px is used.

The red curve in Fig. 6 shows the optical delay during our measurements. According to the theoretical estimation, our shortest delay line (i.e., $\Delta t = 300$ ps) is inappropriately long for measurements of velocities exceeding 300 km/s. To improve this, a shorter illumination pulse should be used. On the other hand, the velocities lower than 2 km/s requires a longer delay line, which can be most appropriately realized with optical fibers.

5 Conclusion

We have presented a developed two-frame shadowgraph method and subsequent data processing that enables 2D measurements of instantaneous velocities of fast laser-induced phenomena in transparent media. Here, a special emphasis has been given to the minimization of the systematic error due to alignment of both images, and to the determination of 2D velocity distribution from captured image pairs. By using this method, we have measured the 2D velocity of plasma expansion and shock wave propagation in air. These experimental results confirm that the developed method is suitable for 2D velocity measurements from the very beginning of the laser-induced breakdown to the times, when the excitation laser radiation has already ended.

Using the shock wave axial-velocity measurements, we have shown that an appropriate adaptation of the optical delay between the direct and the delayed probe-pulse is required to obtain accurate velocity estimates. We have discussed two regimes of shock wave development during a laser-induced breakdown event: the plasma-driven shock wave and the propagating shock wave. Our results demonstrate that the latter one can be described by the Jones model of intermediate strength blast wave. By fitting this model to the measured data, we have determined that approximately 13 % of the optical energy was converted into the blast energy of the shock wave.

References

1. C.G. Morgan, Rep. Prog. Phys. **38**, 621 (1975)
2. P.K. Kennedy, D.X. Hammer, B.A. Rockwell, Prog. Quantum Electron. **21**, 155 (1997)
3. D.A. Cremers, L.J. Radziemski, *Handbook of Laser-Induced Breakdown Spectroscopy* (Wiley, Chichester, 2006)
4. A.A. Ilyin, I.G. Nagorny, O.A. Bukin, Appl. Phys. Lett. **96**, 171501 (2010)
5. J.P. Singh, S.N. Thakur, *Laser-Induced Breakdown Spectroscopy* (Elsevier, Amsterdam, 2007)
6. P. Gregorčič, J. Možina, Opt. Lett. **36**, 2782 (2011)
7. J. Možina, J. Diaci, Appl. Phys. B **105**, 557 (2011)
8. M. Lackner, S. Charareh, F. Winter, K.F. Iskra, D. Rüdisser, T. Neger, H. Kopecek, E. Wintner, Opt. Express **12**, 4546 (2004)
9. M. Kandula, R. Freeman, Shock Waves **18**, 21 (2008)
10. A. Vogel, Phys. Med. Biol. **42**, 895 (1997)
11. I. Apitz, A. Vogel, Appl. Phys. A **81**, 329 (2005)
12. A. Vogel, S. Busch, U. Parlitz, J. Acoust. Soc. Am. **100**, 148 (1996)
13. T. Perhavec, J. Diaci, Stroj. Vestn. **56**, 477 (2010)
14. A. Vogel, I. Apitz, S. Freidank, R. Dijkink, Opt. Lett. **31**, 1812 (2006)
15. G.S. Settles, *Schlieren and Shadowgraph Techniques* (Springer, Berlin, 2001)
16. E.A. Brujan, T. Ikeda, K. Yoshinaka, Y. Matsumoto, Ultrason. Sonochem. **18**, 59 (2011)
17. J. Noack, D.X. Hammer, G.D. Noojin, B.A. Rockwell, A. Vogel, J. Appl. Phys. **83**, 7488 (1998)
18. Z.W. Liu, G.J. Steckman, D. Psaltis, Appl. Phys. Lett. **80**, 731 (2002)
19. C. Sánchez-Aké, H. Sobral, M. Villagrán-Muniz, L. Escobar Alarcon, E. Camps, Opt. Lasers Eng. **39**, 581 (2003)
20. P. Gregorčič, R. Petkovšek, J. Možina, J. Appl. Phys. **102**, 094904 (2007)
21. C. Sánchez-Aké, M. Bolaños, C.Z. Ramírez, Spectrochim. Acta B **64**, 857 (2009)
22. C. Sánchez-Aké, D. Mustri-Trejo, T. García-Fernández, M. Villagrán-Muniz, Spectrochim. Acta B **65**, 401 (2010)
23. P. Gregorčič, R. Petkovšek, J. Možina, G. Močnik, Appl. Phys. A, Mater. Sci. Process. **93**, 901 (2008)
24. D.L. Jones, Phys. Fluids **11**, 1664 (1968)
25. A. Masood, M. Sarfraz, Image Vis. Comput. **27**, 704 (2009)
26. R. Tambay, D.V.S. Muthu, V. Kumar, R.K. Thareja, Pramāna **37**, 163 (1991)
27. H. Sobral, M. Villagrán-Muniz, R. Navarro-González, A.C. Raga, Appl. Phys. Lett. **77**, 3158 (2000)
28. G. Taylor, Proc. R. Soc. Lond. Ser. A, Math. Phys. Sci. **201**, 159 (1950)
29. G. Taylor, Proc. R. Soc. Lond. Ser. A, Math. Phys. Sci. **201**, 175 (1950)
30. J. Diaci, J. Možina, Ultrasonics **34**, 523 (1996)